A NEW QUASI-BRITTLE DAMAGE MODEL IMPLEMENTED UNDER QUASI-STATIC CONDITION USING BOND-BASED PERIDYNAMICS THEORY FOR PROGRESSIVE FAILURE

H. N. Yakin, M. R. M. Rejab, Nur A. Hashim, and N. Nikabdullah

ABSTRACT. A novel quasi-brittle damage model implemented under quasi-static loading condition using bond-based peridynamics theory for progressive failure is proposed to better predict damage initiation and propagation in solid materials. Since peridynamics equation of motion was invented in dynamic configuration, this paper applies the adaptive dynamic relaxation equation to achieve steady-state in peridynamics formulation. To accurately characterise the progressive failure process in cohesive materials, we incorporate the dynamic equation with the novel damage model for quasi-brittle materials. Computational examples of 2D compressive and tensile problems using the proposed model are presented. This paper presents advancement by incorporating the adaptive dynamic equation approach into a new damage model for quasi-brittle materials. This amalgamation allows for a more accurate representation of the behavior of damaged materials, particularly in static or quasi-static loading situations, bringing the framework closer to reality. This research paves the way for the peridynamics formulation to be employed for a far broader class of loading condition behaviour than it is now able to.

1. Introduction

For many decades, fracture initiation and propagation has been recognized as an important research topic. Thus, a considerable amount of literature has been published on this topic, including studies that presented smoothed particle hydrodynamics (SPH) [19], element deletions [33], molecular dynamics (MD) [2], cohesive zone finite elements [7,29], and extended finite element (XFEM) approaches [8,34]. However, in the literature related to the mentioned methods, the relative importance of them has been subject to considerable discussion since these methods

---

call for particular nodal enrichment functions and also crack propagation criteria [30, 31]. Furthermore, a fundamental constraint in analyzing problems with discontinuities is that existing computational methods for modeling fractures in continuous materials rely on partial differential equations (PDEs) rooted in classical continuum mechanics theory. As a result, inherent limitations arise.

The Peridynamics (PD) theory was initiated by Silling [30] as an alternative non-local meshless method to model material damage by employing integral in its formulation instead of spatial partial differential equations as in classical continuum mechanics theory. In this theory, the continuous body is divided into finite material points, and the interaction between the material points occur within a certain specified horizon. Thus, in PD theory, the inadequacies of classical local continuum theory for the problems involving discontinuities such as crack are removed, and the crack prediction problems, such as interface delamination and crack swirling, can be naturally solved without preset crack path and extra fracture criteria. There are typically three categories of PD models: bond-based peridynamics (BB-PD) [30], ordinary state-based peridynamics (OSB-PD) [32], and non-ordinary state-based peridynamics (NOSB-PD) [39]. The original version, BB-PD, utilizes a system in which points are connected by bonds through spring-like interactions, with the force response in a bond solely determined by its own deformation.

BB-PD has been used widely to model material damage and failure. PD introduced the concept of material failure by setting a predefined stretch limit, if stretch value between any bond exceeds this value, then the failure occurs [30]. The BB-PD model is more straightforward compared to another version of PD that is state-based PD in modeling, and it is more stable in terms of the crack propagation simulation problem, and that is why it is widely utilised in the analysis of discontinuities [4, 14, 25, 37, 38, 43, 46]. This has been proved by the vast majority of studies on PD specifically BB-PD in the past two decades since its beginning. Casolo and Diana [4] presented two stochastic discrete models for structural glass, in which the distinctive features of such material have been considered; the perfectly brittle nature of its failure; the variability of the strengths associated with a Weibull distribution and the mechanical behavior of the interlayer in the post-elastic response. Latest literature on BB-PD presented by Ma et al. [21] on data-driven algorithm based on Taylor series expansion to define nonlocal influence function of BB-PD and the numerical tests showed that the proposed method has the ability to accurately regress the nonlocal influence function. Du et al. proposed an improved bond-based peridynamics (iBB-PD) to model crack initiation, propagation and coalescence processes of rocks under uniaxial compression [6]. The elastic-brittle model and the elastic-brittle-plastic model were introduced in the improved Prototype Miroelastic Brittle constitutive model as the constitutive model of the bond under tension and compression, respectively. Prudhomme and Diehl presented two methods, the so-called extended domain method and variable horizon method, to enforce boundary conditions within the non-local BB-PD model [25].

For this reason, the failure process in such materials is extremely brittle, and the progressive failure process in cohesive materials is rarely accurately described [1, 35, 44]. The study of damage models gained momentum only after

Gerstle et al. [9] acknowledged this limitation. A considerable amount of literature has been published on bilinear bond model [13, 23, 26, 47, 48]. Zaccariotto et al. characterised every single bond by a bilinear relationship between the scalar value of the pairwise force function and the bond stretch in order to model an elastic progressively damaged material [47]. Using a bond-based linear peridynamic model in two dimensions, Zhang et al. offer a fast piecewise bilinear collocation approach [48]. The relationship between the nodes was suggested to be represented by a bilinear law by Rossi et al. In previous iterations of the DEM, this law was successfully implemented by the authors. Uniaxial tensile simulations of sandstone specimens exhibit good agreement with actual data, proving the validity of the bilinear model used in Rossi et al. [26]. Niazi et al. [23] studied crack nucleation in a plate with a hole under quasi-static loading using bilinear and trilinear PD models. Hobbs [13] employed a bilinear constitutive law, and the sensitivity of the model is tested using two levels of mesh refinement. A number of studies have proposed another method called trilinear [23, 40, 43–45]. There are, however, certain difficulties in establishing the parameters of such bond models, and the acquired results are not very satisfying. Therefore, developing a suitable bond model for the BB-PD theory is essential for investigating fracture issues in quasi-brittle materials.

The governing equation in PD utilises explicit time integration which causes some difficulties when it comes to problems involving quasi-static loading. Therefore, there exists a demand to acquire steady-state solutions with the object of validating the PD predictions against experimental measurements. Kilic et al. presented an extension of dynamic relaxation methods for obtaining steady-state solutions of nonlinear PD equations. Huang et al. [15] presented an extended BB-PD approach and an evaluation on the capability of the proposed numerical PD method to qualitatively and quantitatively capture the quasi-static elastic response, non-propagating and propagating crack problems of materials and structures. Rabczuk et al. [27] introduced a contact algorithm and artificial damping in the dual-horizon PD. The artificial damping coefficient can be used to model the quasi-static experiment. Luo et al. [20] proposed a model with an explicit adaptive dynamic relaxation method in this study by using a non-ordinary state-based peridynamics. Wu et al. [42] invented a new intermediately-homogenized peridynamic (IH-PD) model of concrete and managed to efficiently predict quasi-static crack propagation in concrete. Jo et al. [17] proposed the two-grid based sequential analysis algorithm of implicit PD formulation. However, this is quite complicated to be implemented. Tong et al. [35] came out with an idea of a new damage model proposed in BB-PD formulation to better represent the progressive failure process in brittle materials. However, the implementation is not incorporated in the quasi-static environment.

In this paper, a new quasi-brittle damage model implemented under quasi-static condition using BB-PD theory for progressive failure is presented for the first time. To the best of the authors' knowledge, there are no published studies available which implemented this new damage model in the quasi-static environment. The layout of the paper is as follows. Section 2 provides the formulation of Bond-based Peridynamic, including the bond stretch and micro-elastic constant. Section 3 provides the formulation of Adaptive Dynamic Relaxation use in this proposed

model. Through numerical examples presented in Section 5, the proposed algorithm is verified as well as the accuracy and efficiency of the proposed method for quasi-static damage model. Finally, conclusions are drawn in Section 6. It is to be noted that the formulation is implemented in a Matlab code.

2. Bond-based Peridynamics

Silling at Sandia introduced the bond-based peridynamics (BB-PD) [30], which serves as the foundational version of PD theory. In BB-PD, the connection of one material point to another material point acts like spring forces as in Figure 1.

The interactions between material points depend on the relative displacement of the interacting material point pair and are independent of all other local conditions. This specifies that the connection between two material points are insensitive to the states of other material point. In the PD method, the horizon size, δ refers to a characteristic length scale that defines the range of interactions between material points. It plays a crucial role in capturing the non-local behavior of the material and distinguishes PD from classical continuum mechanics (CCM), which is based on local interactions. The physical meaning of the horizon size can be understood in terms of the neighborhood of influence around each material point. Within the horizon size distance, represented by the dotted green lines in Figure 1, a material point interacts with its neighboring points, exchanging forces and displacements.
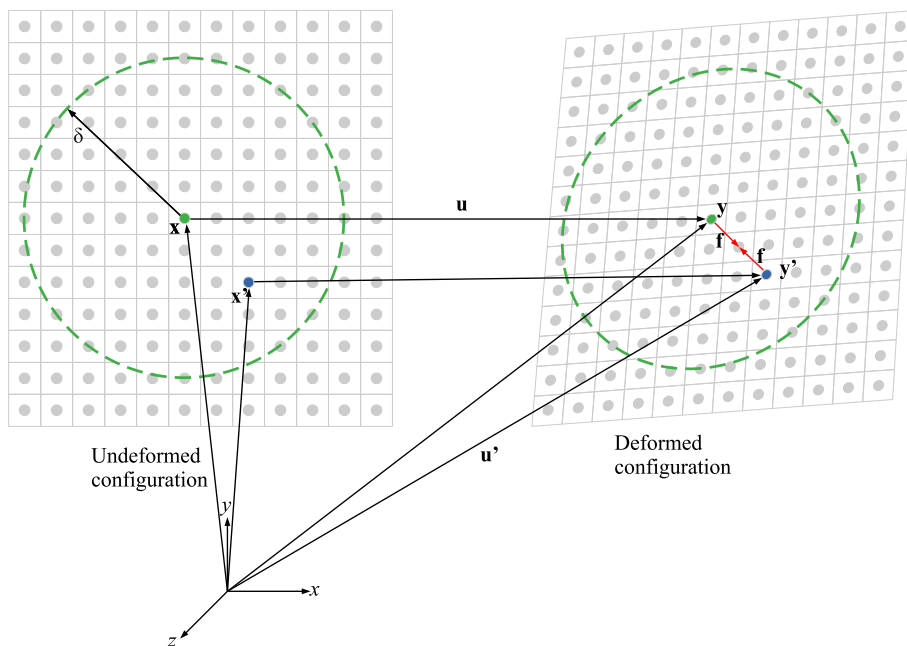

FIGURE 1. Bond-based Peridynamics with horizon size denoted as δ.

These interactions extend beyond the immediate neighboring points, incorporating a larger region around the material point. In CCM, the governing equations are typically formulated based on local spatial derivatives. However, in PD, the formulation is non-local, taking into account the entire deformation field within the horizon size. This non-locality allows PD to effectively capture long-range effects such as cracks, fractures, and other discontinuities without the need for explicit boundary conditions or tracking of interfaces. The choice of the horizon size has significant implications for the behavior of the PD model. A smaller horizon size leads to a more localized interaction, where material points primarily affect their immediate neighbors. On the other hand, a larger horizon size encompasses a larger region, enabling long-range interactions and capturing more global behavior. It is important to note that the horizon size is not an inherent material property but rather a modeling parameter that needs to be carefully chosen. The selection of an appropriate horizon size depends on the specific application, material properties, and desired level of accuracy. Different materials may require different horizon size lengths to accurately represent their behavior. In the PD method, the horizon size determines the range of interactions between material points. The bond constant, representing the stiffness and strength of bonds, is influenced by both the horizon size and material properties, as in Equation (3.1). A smaller horizon size and higher bond constant generally result in increased stiffness and a higher bulk modulus. Conversely, a larger horizon size and lower bond constant tend to promote a softer material response and potentially lower bulk modulus. Additionally, the critical stretch value, representing the material's failure limit, is influenced by both the horizon size and bond constant, as they affect the ability of the material to sustain deformation before failure (see Equation (3.2)). In BB-PD, the equation of motion at the reference configuration at time t is expressed as below [30]

$$\rho\ddot{\mathbf{u}}(\mathbf{x}, t) = \int_R \mathbf{f}\left[\mathbf{u}(\mathbf{x}', t) - \mathbf{u}(\mathbf{x}, t), \mathbf{x}' - \mathbf{x}\right] dV_{\mathbf{x}'} + \mathbf{b}(\mathbf{x}, t),$$

where ρ denotes the mass density, $\ddot{\mathbf{u}}$ is the acceleration of material point $\mathbf{x}$ at time t, R is the region, $\mathbf{f}$ is density force, $\mathbf{u}$ is displacement of material point $\mathbf{x}$ at time t, $\mathbf{x}'$ is material point that interact with material point $\mathbf{x}$, $dV_{\mathbf{x}'}$ is volume of material point $\mathbf{x}'$, $\mathbf{b}(\mathbf{x}, t)$ is body force per unit volume of material point $\mathbf{x}$. The PD pairwise force density function for homogeneous and isotropic materials can be approximately expressed as:

$$\mathbf{f}\left[\mathbf{u}(\mathbf{x}', t) - \mathbf{u}(\mathbf{x}, t), \mathbf{x}' - \mathbf{x}\right] = \mathbf{f}(\boldsymbol{\eta}, \boldsymbol{\xi}) = \frac{\boldsymbol{\eta} + \boldsymbol{\xi}}{|\boldsymbol{\eta} + \boldsymbol{\xi}|} cs,$$

where

$$\boldsymbol{\xi} = \mathbf{x}' - \mathbf{x},$$

and

$$\boldsymbol{\eta} = \mathbf{u}' - \mathbf{u},$$

where $\boldsymbol{\xi}$ stand for the relative position vector of two material points $\mathbf{x}$ and $\mathbf{x}'$, $\boldsymbol{\eta}$ is the relative deformation vector of two material points $\mathbf{x}$ and $\mathbf{x}'$ in the reference

configuration. $\xi + \eta$ is the current relative deformation vector, s is bond stretch which can be defined as

$$s = \frac{|\boldsymbol{\xi} + \boldsymbol{\eta}| - |\boldsymbol{\xi}|}{|\boldsymbol{\xi}|},$$

and c is the micro-elastic constant that represents the bond stiffness which can be expressed as

$$c = \begin{cases} \frac{12E}{\pi \delta^4}, & \text{3D}, \\ \frac{9E}{\pi h \delta^3}, & \text{2D plane stress}, \\ \frac{48E}{5\pi h \delta^3}, & \text{2D plane strain}, \end{cases}$$

where E is the elastic modulus of material, h is the thickness, Poisson's ratio value is fixed to $\frac{1}{4}$ for the plane strain and 3D, and $\frac{1}{3}$ for the plane stress.

One notable drawback of PD is the parameter sensitivity, where simulation results strongly depend on the values chosen for various model parameters. This sensitivity is evident in the horizon size parameter, a characteristic length scale determining particle interactions. Selecting an appropriate horizon parameter is crucial, as a small value can result in excessive noise and inability to capture long-range interactions, while a large value can lead to excessive smoothing and loss of localized behavior. Additionally, material parameters such as elastic modulus and Poisson's ratio must be accurately determined through experimental testing to avoid unrealistic or unreliable simulation outcomes. Another factor contributing to parameter sensitivity is the time step size, which influences stability and accuracy. However, the permissible time step size is often constrained by stability conditions, imposing limitations on the time integration scheme. Furthermore, peridynamics simulations tend to be computationally expensive due to the explicit consideration of non-local interactions, making large-scale simulations and parameter studies time-consuming and resource-intensive. Moreover, the lack of standardized calibration procedures in peridynamics poses challenges for comparing and validating results across studies, affecting the reliability and reproducibility of simulation outcomes. To address these issues, ongoing research focuses on improving parameter estimation techniques, adaptive horizon selection, and more efficient numerical algorithms.

3. Adaptive Dynamic Relaxation (ADR)

The dynamic form is the original form that was utilised in the PD mathematical formulation. Thus, this brings some difficulties when simulating problems or experiments involving static or quasi-static motion. Hence, there exists a necessity to attain the steady-state solutions for validation purpose of PD method against experimental observations. Kilic provided an extension of dynamic relaxation techniques in order to achieve steady-state solutions to nonlinear PD equations in his presentation [18] . This approach was derived from the dynamic relaxation method by injecting an artificial damping into the system; nevertheless, it is still not always feasible to predict which damping coefficient will have the most impact. The concept of adaptive dynamic relaxation, where the damping coefficient changes in

each iteration step, was implemented by Papadrakakis and Underwood [24,36]. By ignoring the body force, $\mathbf{b}$, the equation of motion can be cast into set of ordinary differential equations that become suitable for dynamic relaxation by removing the acceleration term and introducing a fictitious diagonal density and damping matrix that is proportional to the density matrix as

$$\ddot{\mathbf{U}}(\mathbf{X}, t) + \zeta\dot{\mathbf{U}}(\mathbf{X}, t) = \mathbf{\Psi}^{-1}\mathbf{M}(\mathbf{U}, \mathbf{X}),$$

where $\mathbf{\Psi}$, ζ, and $\mathbf{M}$ are the fictitious diagonal density matrix, the damping coefficient, and external force, respectively, where the first two parameters may be derived using Greschgorin's theorem [36]. The vectors X and U include the initial position and displacement of the material points, respectively, and they may be represented as [36]

$$\mathbf{X}^T = \{\mathbf{x}_1, \mathbf{x}_2, ..., \mathbf{x_N}\},$$

and

$$\mathbf{U}^T = \{\mathbf{u}(\mathbf{x}_1, t), \mathbf{u}(\mathbf{x}_2, t), ..., \mathbf{u}(\mathbf{x}_N, t)\},$$

where N refers to the total number of material points. Next-time-step velocities can be calculated using central-difference explicit integration, as

$$\dot{\mathbf{u}}^{n+1/2} = [(2 - \zeta\Delta t)\mathbf{u}^{n-1/2} + 2\Delta t\mathbf{\Psi}^{-1}(\mathbf{M})^n]/[2 + \zeta\Delta t],$$

$$\mathbf{u}^{n+1} = \mathbf{u}^n + \Delta t\dot{\mathbf{u}}^{n+1/2},$$

where n represents the nth iteration and Δt is the magnitude of the time step. When doing dynamic relaxation, using a time step size of ($\Delta t = 1$) as the optimal option is recommended [18]. Due to the absence of information on the velocity field at $t^{-1/2}$, the previously given expression cannot be utilised to initiate the integration; nevertheless, the process may start by using

$$\dot{\mathbf{u}}^{1/2} = \frac{\Delta t\mathbf{\Psi}^{-1}(\mathbf{M})^0}{2}.$$

There is no need for the physical interpretation of the density matrix, $\mathbf{\Psi}$, damping coefficient ζ, or time step size, Δt. They may be chosen for their ability to hasten the process of convergence. Gerschgorin's theorem is the basis of the most used approach for selecting a density matrix, which can be expressed as [36],

$$\mathbf{\Psi}^{-1} = \frac{1}{4}\Delta t^2 \sum_j |k_{ij}|,$$

where i is the corresponding material point and j is the material point connected to the corresponding material point i and k_{ij} calculated as [22]

$$k_{ij} = 5\pi\delta^2 bc,$$

where bc represents the bond constant and is written as

(3.1) $$bc = \frac{18K}{\pi\delta^4},$$

where K denotes the bulk modulus. The damping coefficient ζ, which is usually written as

$$\zeta^n = 2\sqrt{((\mathbf{U}^n)^T \mathbf{K}^n \mathbf{U}^n)/((\mathbf{U}^n)^T \mathbf{U}^n)},$$

where $\mathbf{K}^n$ is the diagonal stiffness matrix and ith component can be computed by

$$K_{ii}^n = -((\mathbf{M})_i^n/\mathbf{\Psi}^{-1} - (\mathbf{M})_i^{n-1}/\mathbf{\Psi}^{-1})/(\Delta t \dot{\mathbf{U}}_i^{n-1/2}).$$

It has been shown that critical stretch is a function of the horizon size. The physical material characteristics, type of loadings, length scale, and computational cut of radius are all affected by the horizon size. For linear elastic brittle materials with a given critical energy release rate, G_c, this straightforward connection gives the value of critical stretch value, s_{cr}. If the material exhibits time-dependant nonlinear behaviour such as viscoplasticity, a single critical stretch value, s_{cr} is not a viable failure criterion.

$$(3.2) \qquad s_{cr} = \begin{cases} \sqrt{\dfrac{G_c}{(3\mu + (\frac{3}{4})^4(\kappa - \frac{5\mu}{3}))\delta}} & \text{3-D,} \\[3ex] \sqrt{\dfrac{G_c}{(\frac{6}{\pi}\mu + \frac{16}{9\pi^2}(\kappa - 2\mu))\delta}} & \text{2-D.} \end{cases}$$

where G_c is the energy required to open a new fracture surface of unit area, namely critical energy release rate, μ is history dependant scalar-valued as in Equation (4.1), κ is the bulk modulus. Horizon size is one of the features in PD theory where it introduces a length parameter that specifies the size of the region where nonlocal interactions can occur. It is to be noted that ADR is a method to ensure convergence of dynamic solution to static solution. In the ADR method for crack propagation, it is necessary to halt crack propagation with the same load as the crack progresses. The system must then reach a steady-state condition before allowing the crack to continue growing. By introducing an artificial damping to the system, the solution is guided to the steady-state solution as fast as possible. In this context, steady-state solutions refer to situations where the displacement of a collocation point converges to a stable or static value after a specific number of time steps. In our analysis, the damping coefficient is evaluated in every iteration in order to get the system to reach steady state condition. By doing this, the damping coefficient adopted will not alternate the final results.

4. Quasi-Brittle (QBR) damage model

In order to better understand the progressive failure process in cohesive brittle materials, the bond damage model was introduced [35] within the context of the BB-PD theory. The acronym QBR stands for "Quasi-Brittle" and was used to describe this paradigm. Rots [28] performed a similar series of experiments in the 1980s to compare the suitability of different mathematical functions; linear, exponential and power, in order to reproduce the global load-deflection plot. From the experiment, it was found that exponential function was the most consistent compared to the experimental results. Based on this experimental background, some authors have used the exponential law to analyze tensile softening in concrete

[5,11,12,40,44,49]. To better understand the bond mechanical reaction in cohesive quasi-brittle materials, the following model is presented

$$f = \begin{cases} cs, & s < s_{cr}, \\ cs_{cr}[exp(-k\frac{s-s_{cr}}{s_{cr}}) + \alpha\frac{s-s_{cr}}{s}], & s > s_{cr}, \end{cases}$$

where k is the bond force reduction parameter, and α is the bond residual force parameter which is taken as 0.01 and 0 throughout this analysis [35]. In this model, the bond status coefficient, μ can be evaluated as

$$\mu(\boldsymbol{\xi}) = \begin{cases} 1, & s \leqslant s_{cr}, \\ \frac{f}{cs_{cr}}, & s > s_{cr}, \end{cases}$$

which can be rewritten as

$$(4.1) \qquad \mu(\boldsymbol{\xi}) = \begin{cases} 1, & s \leqslant s_{cr}, \\ \exp(-k\frac{s-s_{cr}}{s_{cr}}) + \alpha\frac{s-s_{cr}}{s}, & s > s_{cr}. \end{cases}$$

This method was introduced as in the classical bond model, the bond force increases linearly with the bond stretch and suddenly drops to zero when the stretch value of the bond reaches its critical value. The classical model has been widely used for modeling fracture problems in linear-elastic brittle materials but it is not suitable for most cohesive brittle materials such as rocks and cement-based materials since the macroscopic failure is generally a progressive process. Algorithm 1 demonstrates the pseudo-code of the implementation of the new QBR damage model implemented under quasi-static condition using BB-PD theory for progressive failure with Matlab code.

Given the progressive nature of macroscopic failure in cohesive brittle materials, such as rocks and cement-based materials, it is often observed that damage accumulation and fracture under compression tend to be gradual. Conversely, under uniaxial tension, fracture is typically characterized by rapid and catastrophic failure. However, it is crucial to acknowledge that these tendencies may vary depending on factors such as the specific material properties, loading conditions, and other relevant parameters. Therefore, while it is generally true that compression exhibits progressive damage accumulation while tension displays rapid fracture, it is essential to consider the influence of various factors on the actual behavior of the material. The utilization of the present damage model stems from the inherent limitation of the conventional bond model, wherein the bond force exhibits linear growth with bond stretch until abruptly vanishing at the critical bond stretch value. This limitation prompted the adoption of the implemented damage model, which aligns more closely with experimental findings that adhere to the exponential rule as reported by Tong et al. (2020). The pseudo-code for executing the novel quasi-brittle damage model under quasi-static conditions is outlined in Algorithm 1.

Algorithm 1 Pseudo-code of the implementation of the proposed model.

1: **for** $lstp = 1$ to $lstp_n$ **do**
2:     **for** $i = 1$ to I_n **do**
3:         **for** $j = 1$ to m **do**
4:             relative position, $\boldsymbol{\xi} = \mathbf{x}_j - \mathbf{x}_i$.
5:             relative displacement, $\boldsymbol{\eta} = \mathbf{u}(\mathbf{x}_j, t) - \mathbf{u}(\mathbf{x}_i, t)$.
6:             bond stretch, $s(t, \boldsymbol{\eta}, \boldsymbol{\xi}) = \frac{\|\boldsymbol{\eta}+\boldsymbol{\xi}\| - \|\boldsymbol{\xi}\|}{\|\boldsymbol{\xi}\|}$.
7:             critical stretch value, $s_{cr} = \sqrt{\frac{G_c}{(\frac{6}{\pi}\mu + \frac{16}{9\pi^2}(\kappa - 2\mu))\delta}}$.
8:             constant micromodulus, $c = \frac{12k'}{\pi h \delta^3}$.
9:             history-dependent scalar valued function, $\mu(\boldsymbol{\xi}) = \begin{cases} 1 & s \leqslant s_{cr}, \\ \frac{f}{cs_{cr}} & s > s_{cr}. \end{cases}$
10:            bond force, $f = \begin{cases} cs, & s < s_{cr}, \\ cs_{cr}[exp(-k\frac{s-s_{cr}}{s_{cr}}) + \alpha\frac{s-s_{cr}}{s}], & s > s_{cr}, \end{cases}$
11:            pairwise force function, $\mathbf{f}(\boldsymbol{\eta}, \boldsymbol{\xi}) = f\frac{\boldsymbol{\eta}+\boldsymbol{\xi}}{\|\boldsymbol{\eta}+\boldsymbol{\xi}\|}$.
12:            diagonal stiffness matrix, $K_{ii}^n = -((\mathbf{M})_i^n/\boldsymbol{\Psi}^{-1} - (\mathbf{M})_i^{n-1}/\boldsymbol{\Psi}^{-1})/(\Delta t \dot{\mathbf{U}}_i^{n-1/2})$.
13:        **end for**
14:        summation of pairwise force function, $\mathbf{L}(\mathbf{x}_i) = \sum_{j=1}^m \mathbf{f}(\boldsymbol{\eta}, \boldsymbol{\xi})V_j$.
15:        acceleration, $\ddot{\mathbf{u}}(\mathbf{x}_i, t) = \mathbf{L}(\mathbf{x}_i) + \mathbf{b}(\mathbf{x}_i)/\rho(\mathbf{x}_i)$.
16:        velocity, $\dot{\mathbf{u}}(\mathbf{x}_i, t + \Delta t) = \dot{\mathbf{u}}(\mathbf{x}_i, t) + \ddot{\mathbf{u}}(\mathbf{x}_i, t)\Delta t$.
17:        displacement, $\mathbf{u}(\mathbf{x}_i, t + \Delta t) = \mathbf{u}(\mathbf{x}_i, t) + \dot{\mathbf{u}}(\mathbf{x}_i, t + \Delta t)\Delta t$.
18:    **end for**
19: **end for**

---

5. Numerical examples

Three examples are carried out here to verify and demonstrate the applicability of the new quasi-brittle damage model implemented under quasi-static condition using BB-PD theory for progressive failure. The validation of the proposed model is demonstrated by comparing its predictions with the results from the experimental observations.

5.1. Isotropic plate with a hole under uniaxial tension. For the purpose of demonstrating the capabilities of the proposed damage model, an isotropic plate that has a hole in the centre and is subjected to to quasi-static tensile loading along its horizontal edges [22] is studied here. It is to be noted that the analysis started without any existing failure in the domain of the model. The dimensions used are as shown in Figure 2; a length, l of 50 mm, a width, w of 50 mm, a thickness, h of 0.5 mm, and a diameter, D of 10 mm for the hole. The plate has the following physical characteristics; a Young's modulus, E of 192 GPa, a Poisson's ratio, ν of $\frac{1}{3}$, and a mass density, ρ of 8000 kg/m^3. By providing a velocity, $\mathbf{v}$ of $\pm$ 2.7541e-7 m/s to the plate, the boundary condition is established. The number of material points in x
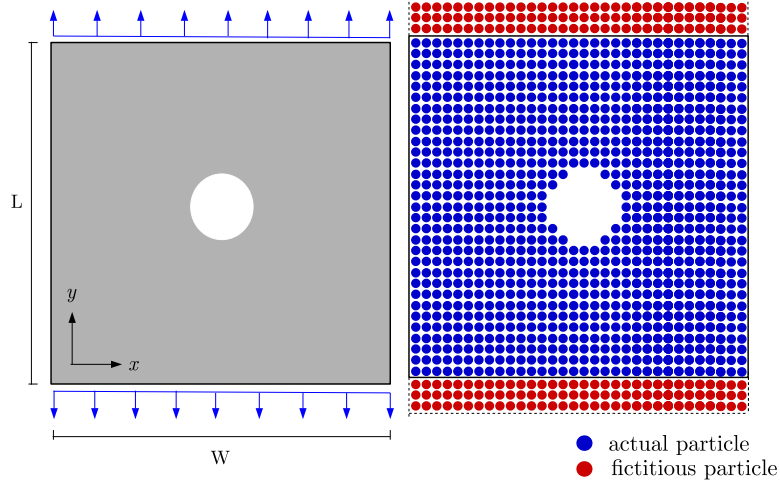
FIGURE 2. The geometry of isotropic plate with a hole and its discretization.

and y-direction is 100, whereas only 1 in z-direction. The spacing between material points, Δ is taken to be 0.5 mm, and the horizon size, δ is equal to $3.015\Delta\mathbf{x}$. When failure is not permitted to occur, the critical stretch value, s_{cr}, is set to 1, and when failure is permitted, it is set to 0.04472. In the absence of failure, the first step is to acquire the displacement field caused by the applied loading and then compare it to the predictions made by the finite element method. Figures 3a and 3b depict the changes in horizontal and vertical displacements along the central x-axis and y-axis, respectively. The proposed model using PD predictions and the

(a) Horizontal displacement.

(b) Vertical displacement.
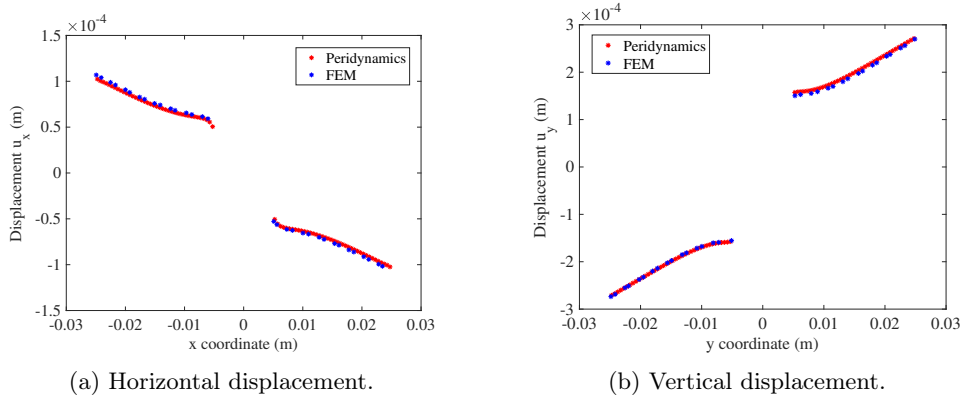
FIGURE 3. The plot of (a) horizontal displacement and (b) vertical displacement along the central axes at the end of one thousand time steps when failure is not permitted to occur.

FEM findings obtained using ANSYS [22] are found to closely accord with one another. This suggests that the values chosen for the PD parameters, such as grid size and horizon size, as well as the volume of the region, provide results that are satisfactory. Failure among the material points is then enabled by setting a critical stretch value of $s_{cr} = 0.04472$, and the evolution of damage is analysed at various time steps once the values of the PD parameters have been established. The failure begins in the form of a fracture at the stress concentration areas, despite the fact that the plate does not have any pre-existing cracks in it. In contrast to the other methods that are currently in use, the PD formulation does not need the presence of pre-existing fractures, which is an unquestionably remarkable quality.

The investigation is carried on by making use of the proposed models under quasi-static [35] conditions with the occurrence of failure. When utilising this damage model, the connection or bond between two nodes does not immediately

(a) Time step = 700.

(b) Time step = 800.
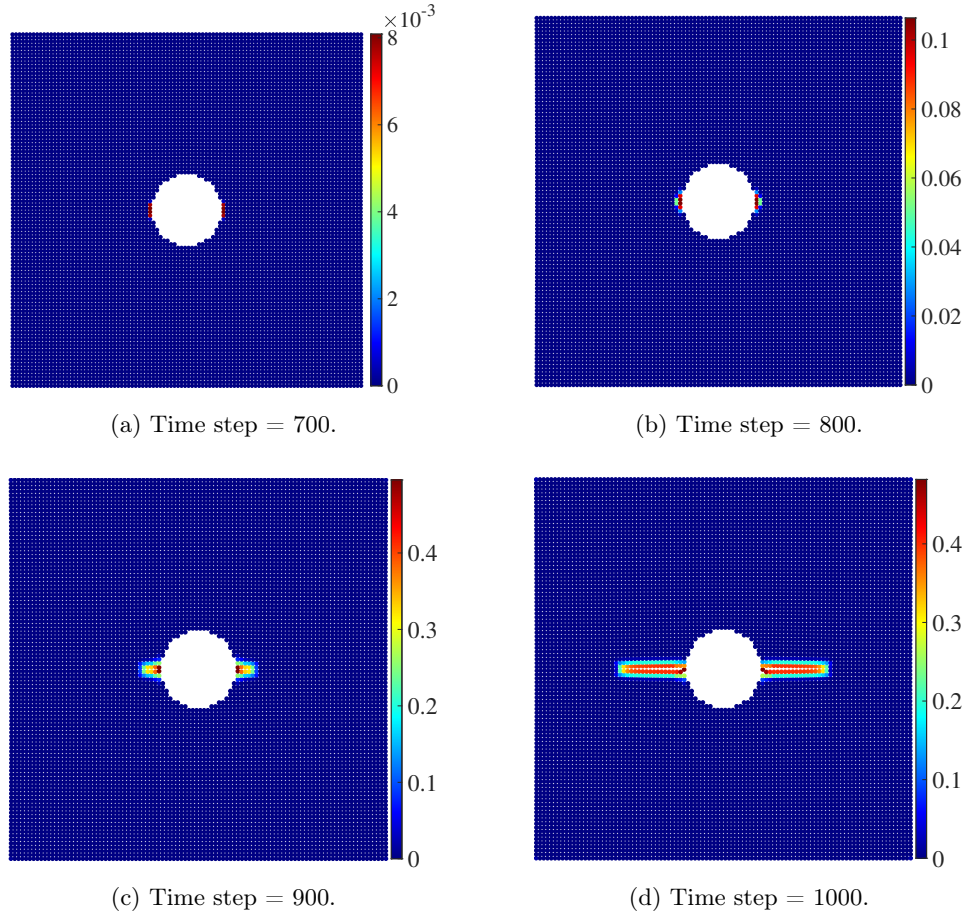
(c) Time step = 900.

(d) Time step = 1000.

FIGURE 4. QBR damage model.

disappear once the value of stretch exceeds the stretch limit, s_{cr} but rather, the force value will decline exponentially until the bond is totally broken and the interconnection is completely severed. Figure 5 illustrates how the suggested model was used to estimate the crack's progression through the material at four distinct time steps: 700, 800, 900, and 1000. According to what is depicted in the figure, the predicted cracks begin at two locations that are diametrically opposed to the hole, spread in a direction that is parallel to the horizontal edges and perpendicular to the loading direction, which is in agreement with what has been observed in the literature [22]. When compared to the damage pattern described in the literature [22], the pattern seen in Figure 4 seems to be more uniform. When modelling brittle materials, which will encounter microcracks during the loading process, the damage model is more realistic than Prototype Microelastic Brittle (PMB) model, particularly when modelling these kinds of materials. As can be observed from Figures 4a, 4b, 4c and 4d, the proposed damage model is capable of accurately modelling both the progressive failure process and the quasi-static loading state.

5.2. 2D rectangular plate with circular hole under uniaxial compression. For the purpose of demonstrating the validity of the suggested model, a two-dimensional rectangular plate with a circular hole and subjected to uniaxial compression is utilised, as illustrated in Figure 5. It is decided to use the experimental result that was published in the literature [16] as a baseline for comparison. The model's geometry can be observed in Figure 5a. These values represent the material characteristics of the plate specimen. According to the experimental data found in the literature [16], the material model was an isotropic linear elastic with a Young's modulus, E of 25 GPa and a Poisson's ratio, $\nu = \frac{1}{3}$. The specimen is discretized evenly into 2331 material points, which are organised in a 105 by 21

(a) Geometric properties of the model.   (b) Applied displacement.
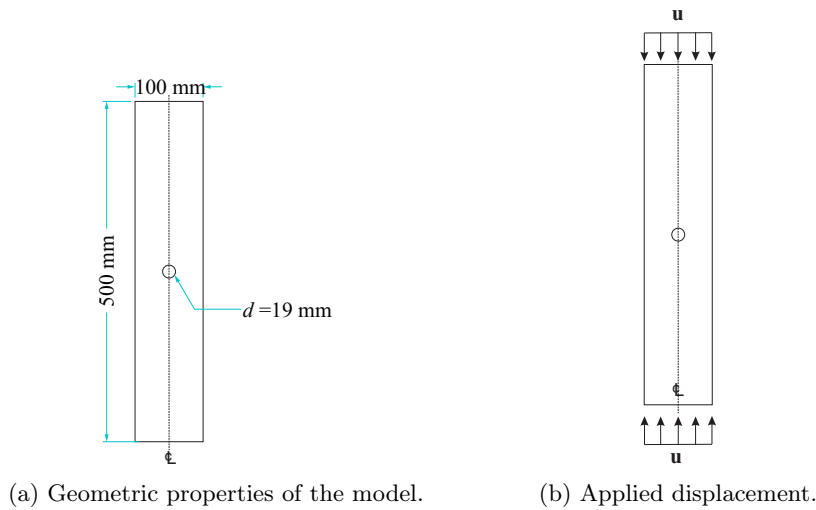
FIGURE 5. Properties of 2D rectangular plate.

regular grid. There are three layers of fictional nodes in both the top and bottom sides of the object, which is where the loading is applied. The material horizon size is set to, $\delta = 3.015\Delta x$. The critical stretch is taken to be 1e-4. The velocity and displacement were applied under uniaxial compression with the value of 2e-8 m/s and 2e-8 m respectively as shown in Figure 5b.

Figure 6 shows the picture of typical observed cracks from the laboratory experiment [16]. The first picture from the left shows that several microcrack initiation points exist from the centre of the specimen where the hole is located. This can be seen from the red-mark drawn on the concrete specimen. The second and third picture from the left in Figure 6 show the zoom-in part of the specimen plate, where in the third picture two major cracks can be observed that starts from the hole; one propagating to the top, and another one propagating to the bottom where the loading is applied. The cracks observed in the third picture from the left in Figure 6 are in the same direction as the loading direction.
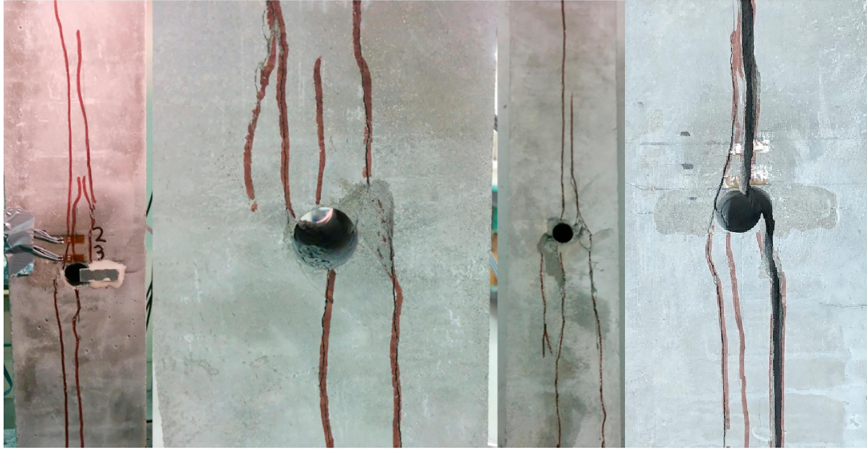

FIGURE 6. Typical observed cracks from experimental results (after [16]).

Figure 7 shows the evolution of the predicted crack propagation in the specimen at different time steps; ts = 2000, 2500, 3000, and 3500, using the proposed model. The geometric idealness of the mesh, with the exception of the hole, suggests that the splitting cracks should originate at the uppermost and lowermost points of the hole along the centerline. However, the observed "wing-like" initiation of the cracks in this analysis can be attributed to the imperfect approximation of the hole, which introduces non-physical stress concentrations along the boundary of the hole. These stress concentrations, caused by the mesh discretization, deviate from the expected behavior seen in reality. In reality, the splitting cracks may initiate away from the centerline due to the existence of various forms of disorder within the material. This implies that the location of crack initiation is influenced by factors beyond the idealized conditions considered in our analysis. It is important to acknowledge
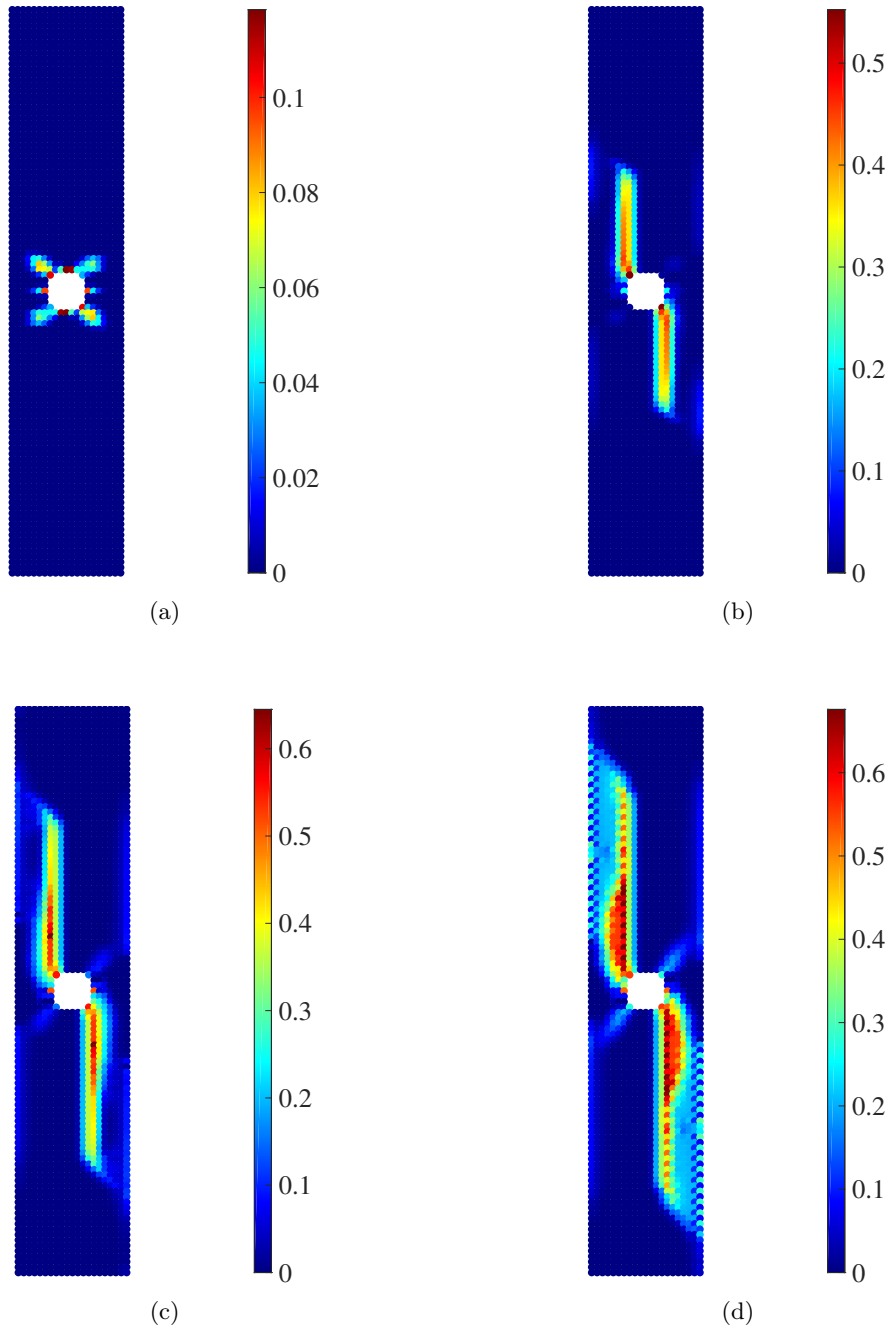
FIGURE 7. Damage evolution of the plate: (a) ts = 2000; (b) ts = 2500; (c) ts = 3000; (d) ts = 3500.

that these deviations in crack initiation are not a result of our findings, but rather a consequence of the unavoidable artificial effects introduced by the discretization of the hole. The damage patterns indicated that the predicted cracks initiate at all four sides of the hole, with two adjacent sides (top left and bottom right) showing a slightly higher level of damage compared to the other two sides. These cracks develop at an angle relative to the horizontal line during the early time steps. Then, the crack trajectories deflect and extend along the vertical line, which agrees well with the experimental observation [16], as shown in Figure 6. The good agreements validate the capability of the new quasi-brittle damage model implemented under quasi-static condition using BB-PD theory for progressive failure.

5.3. 2D rectangular pristine plate under compressive force. To further validate the proposed damage model implemented under quasi-static condition for cracking problems, a 2D rectangular pristine plate under compressive load is analysed. The rectangular plate had an initial height of $h_0 = 8$ mm and width of $w_0 = 4$ mm. The material model was isotropic linear elasticity with a Young's modulus of $E = 190$ GPa, and a Poisson's ratio of $\nu = \frac{1}{3}$. The plate was discretized uniformly, comprising a total of 1,400 material points. Specifically, there were 1,250 material
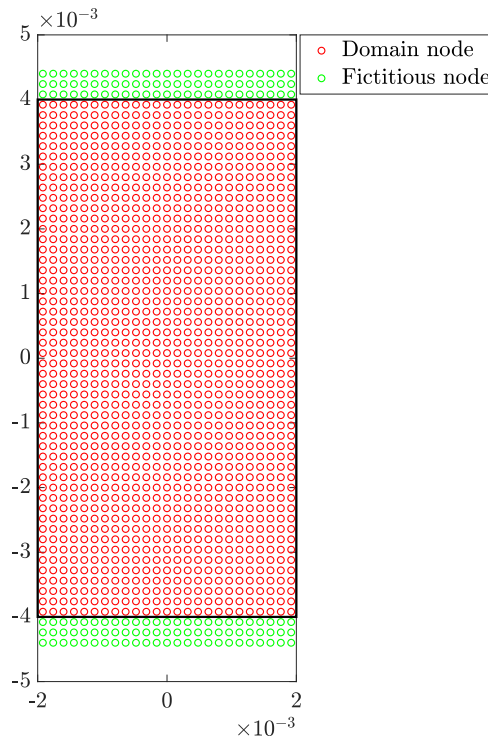

FIGURE 8. Discretisation of the 4 mm × 8 mm specimen using BBPD.

points arranged in a regular grid of 25 by 50 within the plate. Additionally, three layers of fictitious nodes were present on both sides of the plate, accounting for 150 material points where the boundary conditions were applied, as depicted in Figure 8. Moreover, various horizon sizes, denoted as δ, were tested in the analysis. For the first part of the analysis, the value of the critical stretch was set to be large, $s_{cr} = 1$, so that no damage was allowed to happen. In the second part of the analysis, it was allowed for the failure to happen using the exact value of the critical stretch evaluated from the Equation (3.2). The geometrical properties, material properties, and the loading applied in this problem matched up with the experiment in [10]. In this problem, there were two cases of boundary condition applied. For the Case 1 of the boundary condition; the velocity and displacement were applied under uniaxial compression with the value of $\pm 3.33e - 7$ m/s and $\pm 3.33e - 7$ m respectively. In the Case 2 of boundary condition, the velocity and displacement were applied similarly as in Case 1 but with additional horizontal direction with linear increment from the middle towards the side of the specimen. In the experimental setup, the boundary condition applied during the uniaxial compression test deviated from the idealized Case 1 condition. To better capture the actual behavior, an alternative boundary condition, referred to as Case 2, was implemented. In Case 2, a small horizontal force was introduced at the top of the material points while maintaining the uniaxial compression. By incorporating this modification, the boundary condition in the numerical model aligns more closely with the experimental reality. It is worth noting that the true boundary condition in the experiment lies somewhere between Case 1 and Case 2, highlighting the necessity of considering an intermediate scenario for accurately representing the experimental conditions.
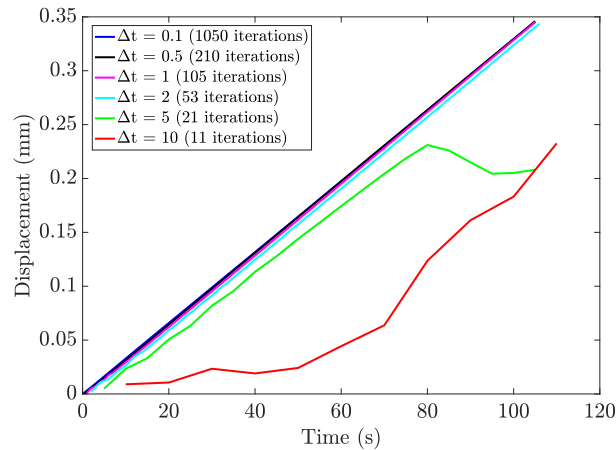

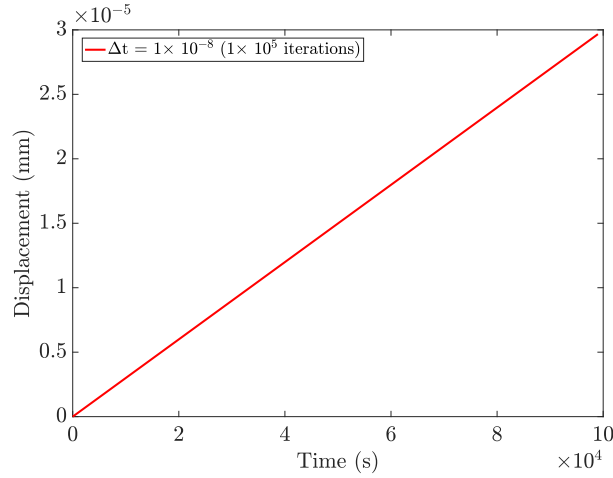FIGURE 9. Displacement vs time with Adaptive Dynamic Relaxation on.

FIGURE 10. Displacement vs time with Adaptive Dynamic Relaxation off.

Figures 9 and 10 depict the plot of displacement versus time for the analysis using the proposed model with and without Adaptive Dynamic Relaxation (ADR) method, respectively. Figure 9 illustrates displacement-time plot for different time step size, Δt that is ranging from 0.1, 0.5, 1, 2, 5, and 10. The analysis in Figure 9 had been run up to time step of 105 s. The plot in Figure 9 shows nearly linear relationship between displacement and time for $\Delta t \leqslant 2$. It is indicated from the Figure 9 that there is a slight slope difference between the $\Delta t = 2$ and $\Delta t = 1$. The tangent from the plot for $\Delta t = 1$, 0.5, and 0.1 yields a very good agreement with the solution without ADR method, indicated in Figure 10. In contrast to Figure 9, the analysis in Figure 10 had been run up to only until 1×10^{-4} s for number of iterations of 1×10^5, which is highly expensive computational time. Generally, smaller time step size (in this case $\Delta t \leqslant 1$) minimises the errors in time-displacement plot. It is concluded that the results generated with smaller value of Δt decreases the errors, however, its efficiency is reduced since they remain computationally expensive. The value of Δt in the analysis without ADR is restricted to a limitation where it should be smaller than a specific value as mentioned in Courant–Friedrichs–Lewy condition in order to produce a stable results. In Figure 10 the Δt was taken to be 1×10^{-8}. From Figures 9 and 10, it can be seen that the tangent of the graph between BBPD with ADR on ($\Delta t \leqslant 2$) and BBPD with ADR off are in a good agreement. In conclusion, the BBPD with ADR produce a good agreement with the explicit analysis and thus BBPD with ADR with $\Delta t = 1$ will be used for the rest of the analysis, as suggested by [18, 20].

Figures 11 and 12 present the variation of vertical and horizontal displacement respectively, using BBPD with different horizon size, Δx and compared with Finite Element Method (FEM) within an in-house Matlab code. The FEM was discretised into 24×48 elements with the same geometrical and material properties. For any
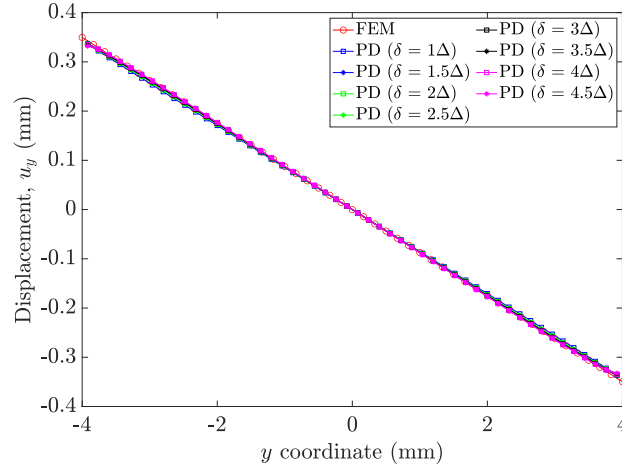
FIGURE 11. Variation of vertical displacement along the $\frac{w_0}{2}$ at the end of 1,050 time steps when failure is not allowed.
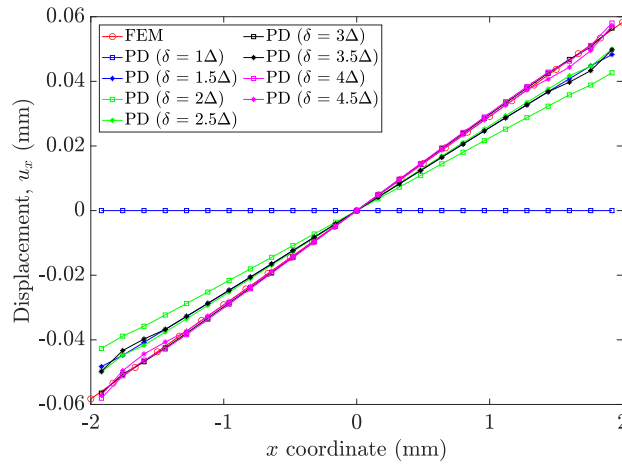

FIGURE 12. Variation of horizontal displacement of the specimen for different horizon size, δ along the $\frac{h_0}{2}$ at the end of 1,050 time steps when failure is not allowed.

specific material point located in the middle of a body, with $\delta = 1\Delta x$ the material point will have only 4 neighbours of material points; for a uniform dicretisation. When $\delta = 1\Delta x$, the diagonal material points will not be included as part of its neighbour. Whereas by selecting δ with the factor of $1.5\Delta x$, the diagonal material points will also be included as neighbour of the material point. Generally, with selection of δ to be in the factor of 1, the horizon produced is in a circle shape (with increasing value of δ), while δ with the factor of 1.5 will make the horizon

size to be in a square shape. From Figure 11, almost all of the chosen δ showed good agreement of vertical displacement compared to the FEM analysis. This was because the prescribed displacement and velocity were applied in vertical direction. From Figure 12, when $\delta = 1\Delta x$, there was no horizontal displacement in the body. This was due to the zero influence of the horizontal displacement applied to the body since the diagonal nodes were not included in the material points' neigbour. When the $\delta = 2\Delta x$, horizontal displacement occur even it is slightly diverged from the FEM displacement plot. The displacement plot when $\delta = 1.5\Delta x$, $2.5\Delta x$, and $3.5\Delta x$ is in between the FEM plot and of the $\delta = 2\Delta x$. Even though the value of $\delta = 1.5\Delta x < \delta = 2\Delta x$, but since the selection of the diagonal material point as part of neighbour brings an extra influence of horizontal effect to the displacement of the main material point. The last three δ; $3\Delta x$, $4\Delta x$, and $4.5\Delta x$, were the nearest plot to the FEM plot. It can be seen that towards the end of the graph, $\delta = 3.5\Delta x$ and $4.5\Delta x$ are straying away from FEM plot, and it seems like too much influence to the horizontal direction will bring an error to the formulation. From this analysis, it can be concluded that the best δ for the formulation of BBPD is $3\Delta x$ as been suggested in the literature [3].
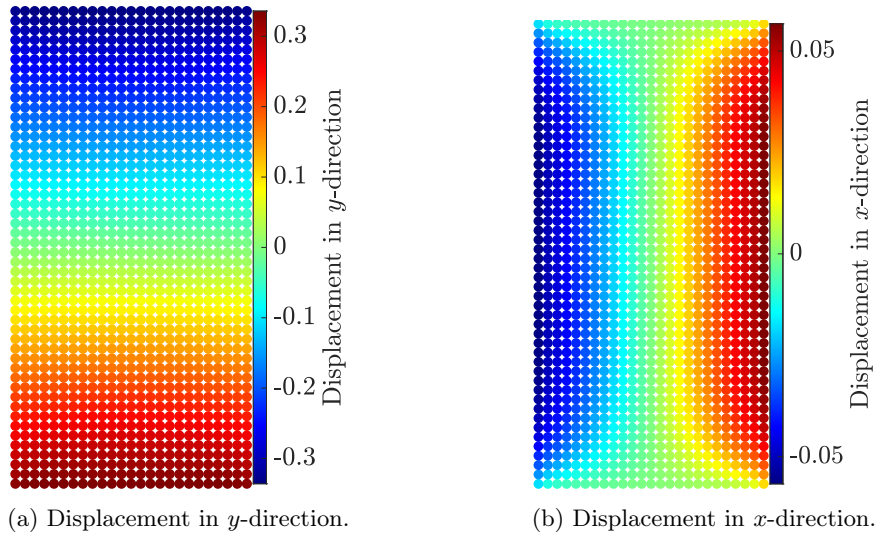

(a) Displacement in y-direction.   (b) Displacement in x-direction.

FIGURE 13. Case 1 boundary condition: Displacement of the specimen in y-direction and x-direction (in mm).

Figures 13a and 13b represent the plot of displacement countour for Case 1 boundary condition in y-direction and x-direction respectively. Figures 14a and 14b represent the plot of displacement countour for Case 2 boundary condition in y-direction and x-direction respectively. From Figures 13a and 14a, the maximum displacement in y-direction is around ± 0.35 mm, which agrees with the result from experiment [10]. The maximum displacement in y-direction from Figures 13b

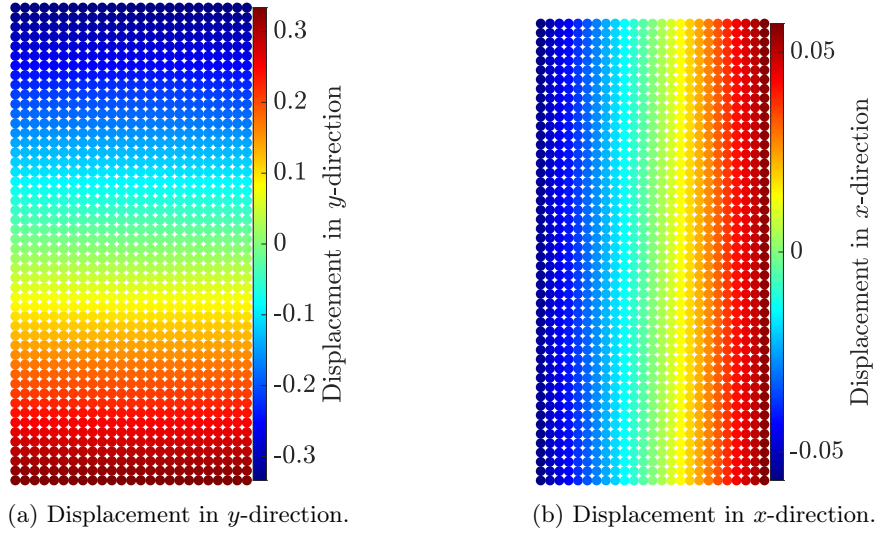(a) Displacement in y-direction.

(b) Displacement in x-direction.

FIGURE 14. Case 2 boundary condition: Displacement of the specimen in y-direction and x-direction (in mm).

and 14b is around ± 0.05 mm, however both of them show different displacement patterns where the x-displacement in Case 2 boundary condition shows uniform displacement along the length of the specimen, whereas the x-displacement in Case 1 boundary condition shows non-uniform pattern along its length. The displacement shape in Case 1 boundary condition shows convex shape when the specimen is compressed. Both of the patterns could be the accurate representation of the deformation in x-direction since the behaviour in x-direction is not observed experimentally.

Figure 15 shows the plot of force vs displacement between Case 1 and Case 2 boundary condition, and experimental results [10]. There are two samples from experimental results plotted in this graph: CMP1 and CMP2. The tangent of the plot in Case 1and Case 2 are in close agreement with the previous experimental results, CMP1 and CMP2. However, the slope between the analysis and experiment is different when the displacement is less than 0.1 mm. This might be due to the reason that there is a slight free movement in the specimen when the loading is applied at the beginning, before the specimen starts to absorb the load. The force value is acquired in the analysis by summation of all the forces in the bonds that cross a cross section, located away from the loading sources.

Figure 16 shows the minimum stretch plot for both of the boundary condition Case 1 and Case 2 at timestep of 1050 s. The minimum stretch plot in Figure 16a shows a non-uniform pattern compared to the same plot for Case 2 boundary condition in Figure 16b. To get a clear pattern of both plots, we plotted again by only specifying the exact range of bond stretch value; removing the smallest value in the plot. Figure 16a is plotted again by only plotting the bond stretch value of
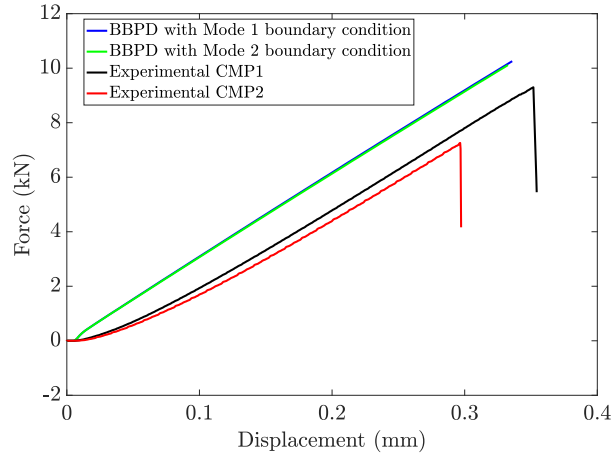
Figure 15. Force vs displacement for BBPD with different boundary condition, and experimental result.

>-0.11, and Figure 16b is plotted again by only plotting the bond stretch value of >-0.0.95 as in Figure 17a and Figure 17b respectively. From these Figures it can be seen that Case 1 boundary condition shows a clear pattern of strain localisation whereas in the Case 2 boundary condition shows a uniform plot of bond stretch.
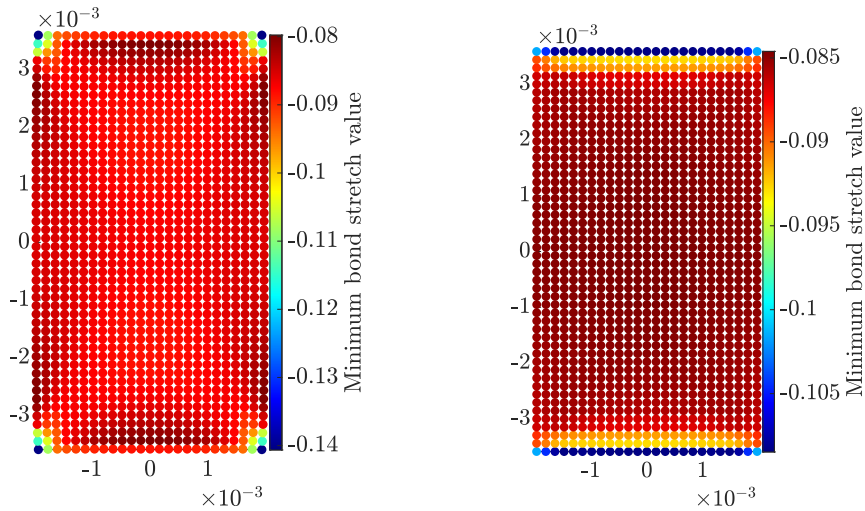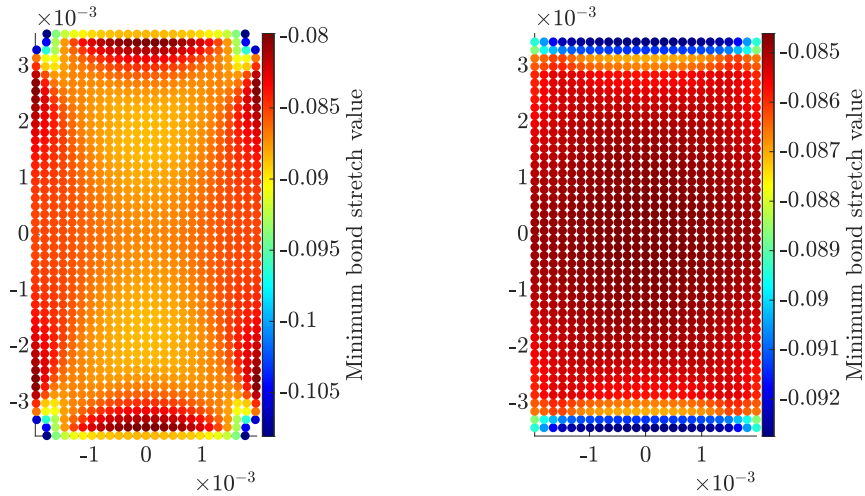

(a) Minimum stretch plot for Case 1 boundary condition at time step 1,050.

(b) Minimum stretch plot for Case 2 boundary condition at time step 1,050.

Figure 16. Minimum stretch plot for different boundary condition.

Comparing the damage plot from the analysis in Figure 18 with experimental results, a slight difference is evident. The analysis indicates a visible conjugate shear fracture, while the experimental results only show a single shear, with the object failing from the top left to the middle right, as depicted in Figures 19 and 20. The differences between the results might occur due to the uncertainties when handling the experiment in the laboratory. When analyzing a pristine object, it is crucial to exercise additional caution to ensure its complete symmetry, thereby maximizing the accuracy of the computer analysis. Discrepancies in results may arise from non-uniform loading conditions within the laboratory setting. Moreover, the small size of the specimens makes it exceedingly difficult to identify any uneven surface that could lead to irregular response under applied loading. Enhancements in the experimental analysis could be achieved by increasing the specimen sizes and implementing strain gauges to ensure uniform loading distribution across all sides of the objects.

In PD, the particular feature that triggers the formation of the localization band is the non-local nature of the bond-based interactions. Unlike traditional continuum models, PD considers interactions between material points within a finite horizon size or neighborhood, allowing for long-range interactions. This non-locality enables the propagation of deformation and damage effects over a larger spatial extent. As a result, when a localized deformation or damage initiates in a small region, it can propagate and spread throughout the material via the bond-based interactions in PD. This mechanism effectively triggers the formation of the

(a) Minimum stretch plot for Case 1 boundary condition at time step 1,050 with neglected value of > -0.11.

(b) Minimum stretch plot for Case 2 boundary condition at time step 1,050 with neglected value of > -0.095.

FIGURE 17. Minimum stretch plot for different boundary condition with negletion part of the stretch value.

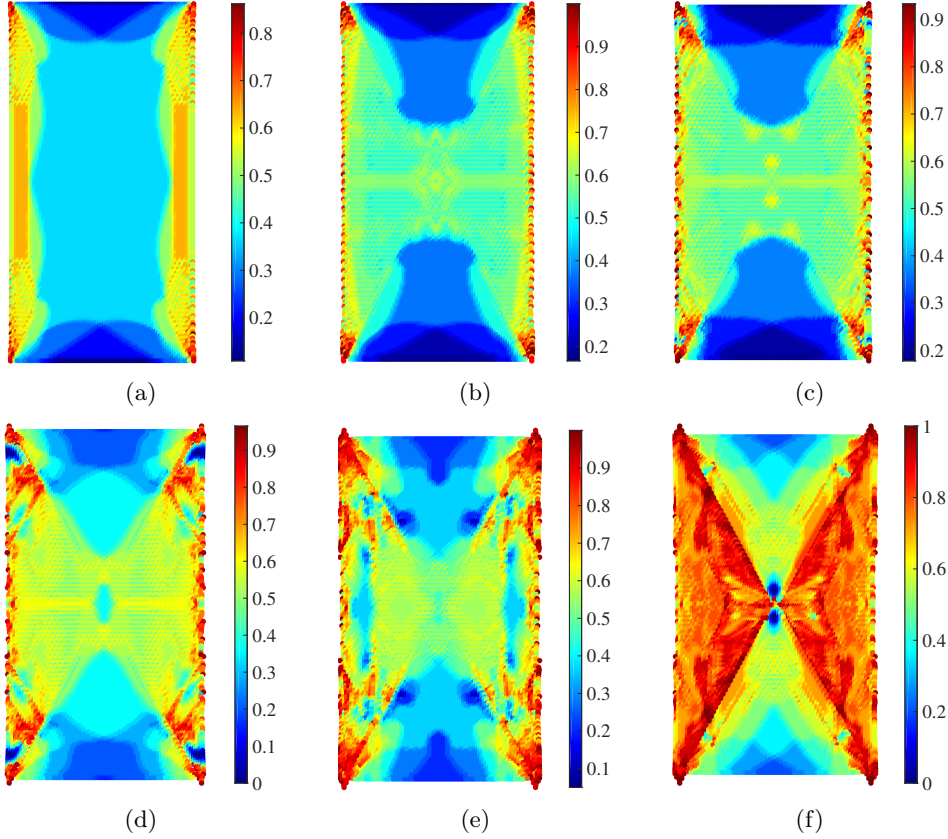FIGURE 18. Damage evolution of the plate: (a) ts = 200; (b) ts = 400; (c) ts = 600; (d) ts = 800; (e) ts = 1000; (f) ts = 1200.

localization band, where intense deformation or damage is concentrated within a narrow zone. Therefore, the key feature of PD that promotes the formation of the localization band is its non-local interaction scheme, allowing for the transmission of deformation and damage effects across larger distances within the material.

5.4. L-shape plate. This example considers an L-shaped panel test as a well-known benchmark problem of the mixed-mode failure for the quasi-brittle structure. The geometric domain and boundary conditions are as depicted in Figure 21. The test was formerly performed by Winkler et al.in [41]. The material parameters are chosen from [35] as Young's modulus, $E = 25.85$ GPa, Poisson's ratio, $\nu = 0.18$, and $G_f = 0.065$ N/mm.

Figure 22 shows a quantitative comparison of the force-displacement curve between our results and those published in [41]. Compared with the experimental results obtained from Winkler et al. [41], the present numerical results obtained by the new quasi-brittle peridynamics with ADR model are in good agreement with the

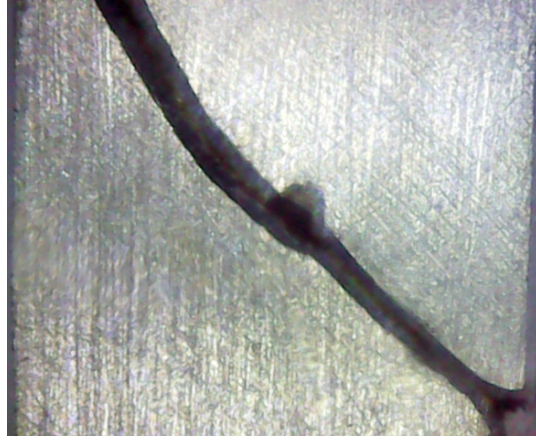FIGURE 19. Failure of the object (after [10]).

FIGURE 20. Failure of the object (after [10]).

experimental results. The variation in force-displacement slopes between numerical analysis and experimental results in the elastic range within the PD method can be attributed to several factors. Firstly, numerical analysis often assumes idealized material behavior, such as linear elasticity, while experimental results reflect the true mechanical response of the material, which can exhibit nonlinear or anisotropic characteristics even within the elastic range. Secondly, differences in discretization and spatial resolution between the numerical model and real-world experiments can affect the accuracy of capturing small-scale features or localized deformations. Additionally, variations in boundary and loading conditions applied in numerical simulations compared to experiments can lead to discrepancies in the force-displacement slopes. Lastly, the use of numerical approximations and algorithms in PD simulations, along with the choice of specific parameters, can introduce errors and impact the agreement with experimental results.

Figure 23 shows the crack propagation mode in L-shape structure test, for displacement of 0.1mm, 0.3mm, 1mm and the experimental of 1mm from [41]. In Figure 23 (a) the initiation of crack propagation starts at the corner of the L-shape. In Figure 23 (b) it can be seen that the crack starts to propagate horizontally away from the corner where it started. In Figure 23 (c) the propagation of the crack nearly reached the end of the specimen. One of the remarkable aspects of PD is its ability to model crack formation and propagation without the need for additional mathematical equations. This feature is of significant interest in the study of material failure, as it enables a more comprehensive understanding of crack behavior and the impact of loading conditions. The inherent flexibility and accuracy of the PD approach allow for a more precise representation of crack formation and propagation, leading to a better understanding of material failure and the development of more effective engineering solutions. The crack propagation in the analysis agrees well with the experimental analysis [41] shown in Figure 23 (d).
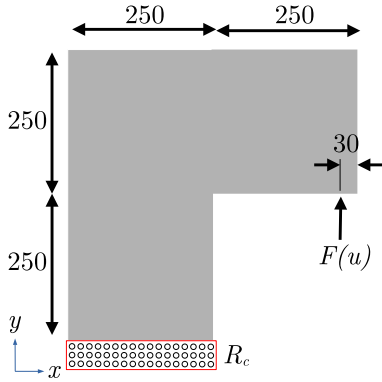
FIGURE 21. The geometry (unit of length: mm) of the L-shaped panel test with its boundary conditions.
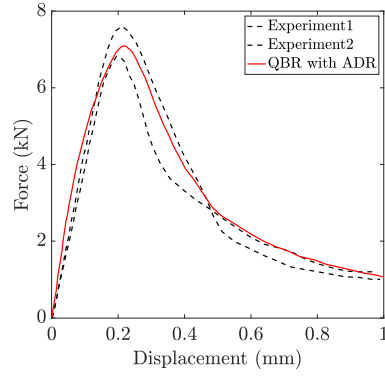

FIGURE 22. The comparison of force–displacement curve of L-shape structure test for experimental data [22] and QBR with ADR. macroscopic

(a) u = 0.1mm

(b) u = 0.3mm

(c) u = 1mm

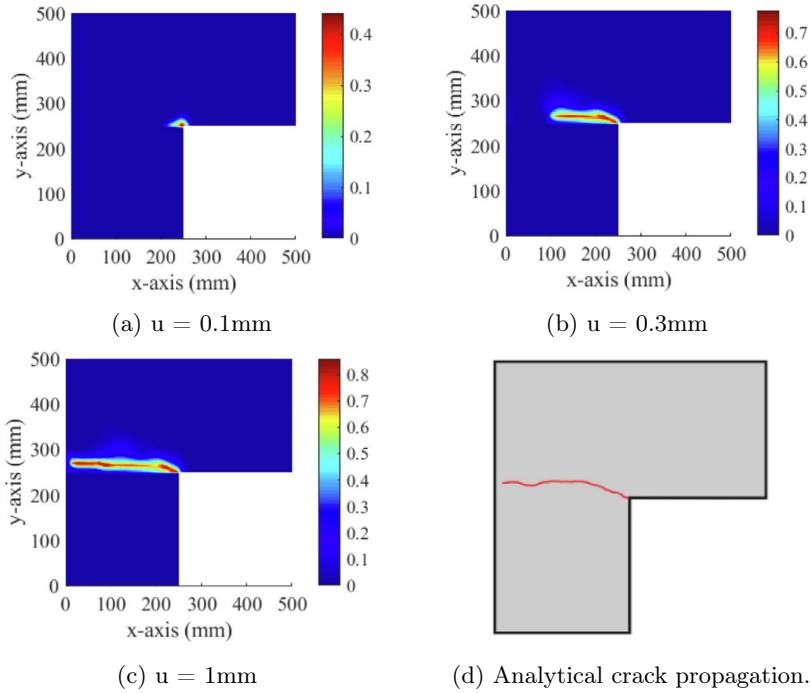

(d) Analytical crack propagation.

FIGURE 23. Crack propagation mode in L-shape structure test.

6. Conclusion

This paper has presented for the first time an extension of the quasi-brittle damage model implemented using BB-PD theory for progressive failure under quasi-static condition. This allows the fracture modeling of a solid body under quasi-static to be modeled with the quasi-brittle damage model. The key contribution of this paper is the combination of the adaptive dynamic equation into the formulation of quasi-brittle damage model using BB-PD. Three numerical examples are presented to validate the effectiveness of this approach. It has been shown that the proposed method is quite capable of simulating quasi-static tensile and compressive load with the damage pattern that agreed well to the literature.

This paper lays the groundwork for quasi-brittle damage model into future research for a broader range of loading combinations and failure modes. It also provides a starting point for the extension of the damage model into the other version of peridynamics such as non-ordinary state based.

References

1. Z. P. Bažant, M. Jirásek, *Nonlocal integral formulations of plasticity and damage: Survey of progress*, Journal of Engineering Mechanics **128**(11) (2002), 1119–1149.
2. H. J. C. Berendsen, J. P. M. Postma, W. F. Van Gunsteren, A. Dinola, J. R. Haak, *Molecular dynamics with coupling to an external bath*, J. Chem. Phys. **81**(8) (1984), 3684–3690.
3. F. Bobaru, Y. Ha, W. Hu, *Damage progression from impact in layered glass modeled with peridynamics*, Open Engineering **2**(4) (2012), 551–561.
4. S. Casolo, V. Diana, *Modelling laminated glass beam failure via stochastic rigid body-spring model and bond-based peridynamics*, Eng. Appl. Fract. Mech. **190** (2018), 331–346.
5. Y. Dong, C. Su, P. Qiao, *An improved mesoscale damage model for quasi-brittle fracture analysis of concrete with ordinary state-based peridynamics*, Theoretical and Applied Fracture Mechanics **112** (2021), 102829.
6. W. Du, X. Fu, Q. Sheng, J. Chen, Y. Du, Z. Zhang, *Study on the failure process of rocks with closed fractures under compressive loading using improved bond-based peridynamics*, Eng. Appl. Fract. Mech. **240** (2020), 107315.
7. M. Elices, G. V. Guinea, J. Gómez, J. Planas, *The cohesive zone model: Advantages, limitations and challenges*, Eng. Appl. Fract. Mech. **69**(2) (2001), 137–163.
8. H. Fan, G. L. Bergel, S. Li, *A hybrid peridynamics-SPH simulation of soil fragmentation by blast loads of buried explosive*, International Journal of Impact Engineering **87** (2016), 14–27.
9. W. Gerstle, N. Sau, S. A. Silling, *Peridynamic Modeling of Plain and Reinforced Concrete Structures*, IASMiRT, SMiRT 18, 2005, 1–15.
10. Q. Halim, N. Nikabdullah, M. R. M. Rejab, M. Rashidi, *Fracture response of La61.4 Al15.9 Ni11.35 Cu11.35 bulk metallic glass subjected to quasi-static compression loading*, Materials Today: Proceedings **27** (2020), 1761–1767.
11. M. Hobbs, T. Dodwell, G. Hattori, J. Orr, *An examination of the size effect in quasi-brittle materials using a bond-based peridynamic model*, Engineering Structures **262** (2022), 114207.

12. M. C. Hobbs, *Three-dimensional peridynamic modelling of quasi-brittle structural elements*, PhD thesis, University of Cambridge. 2021.

13. M. Hobbs, G. Hattori, J. Orr, *Predicting shear failure in reinforced concrete members using a three-dimensional peridynamic framework*, Comput. Struct. **258** (2022), 106682.

14. Y. L. Hu, E. Madenci, *Bond-based peridynamic modeling of composite laminates with arbitrary fiber orientation and stacking sequence*, Composite Structures **153** (2016), 139–175.

15. D. Huang, G. Lu, P. Qiao, *An improved peridynamic approach for quasi-static elastic deformation and brittle fracture analysis*, Int. J. Mech. Sci. **94–95** (2015), 111–122.

16. M. Iskander, N. Shrive, *Fracture of brittle and quasi-brittle materials in compression: A review of the current state of knowledge and a different approach*, Theoretical and Applied Fracture Mechanics **97** (2018), 250–257.

17. G. Jo, Y. D. Ha, *Two-grid based sequential peridynamic analysis method for quasi-static crack propagation*, Eng. Appl. Fract. Mech. **269** (2022), 108549.

18. B. Kilic, E. Madenci, *An adaptive dynamic relaxation method for quasi-static simulations using the peridynamic theory*, Theoretical and Applied Fracture Mechanics **53**(3) (2010), 194–204.

19. M. B. Liu, G. R. Liu, S. Li, *Smoothed particle hydrodynamics - a meshfree method*, Comput. Mech. **33**(6) (2004), 491–491.

20. J. Luo, A. Ramazani, V. Sundararaghavan, *Simulation of micro-scale shear bands using peridynamics with an adaptive dynamic relaxation method*, Int. J. Solids Struct. **130–131** (2018), 36–48.

21. J. Ma, X. Zhou, *Data-driven bond-based peridynamics with nonlocal influence function for crack propagation*, Eng. Appl. Fract. Mech. **272** (2022), 108681.

22. E. Madenci, E. Oterkus, *Peridynamic Theory and Its Applications*, Vol. C, Springer New York, New York, NY, 2014.

23. S. Niazi, Z. Chen, F. Bobaru, *Crack nucleation in brittle and quasi-brittle materials: A peridynamic analysis*, Theoretical and Applied Fracture Mechanics **112** (2021), 102855.

24. M. Papadrakakis, *A method for the automatic evaluation of the dynamic relaxation parameters*, Comput. Methods Appl. Mech. Eng. **25**(1) (1981), 35–48.

25. S. Prudhomme, P. Diehl, *On the treatment of boundary conditions for bond-based peridynamic models*, Comput. Methods Appl. Mech. Eng. **372** (2020), 113391.

26. N. R. Cabral, M. A. Invaldi, R. B. D'Ambra, I. Iturrioz, *An alternative bilinear peridynamic model to simulate the damage process in quasi-brittle materials*, Eng. Appl. Fract. Mech. **216** (2019), 106494.

27. T. Rabczuk, H. Ren, *A peridynamics formulation for quasi-static fracture and contact in rock*, Engineering Geology **225** (2017), 42–48.

28. J. G. Rots, *Computational Modeling of Concrete Fracture*, PhD thesis, Delft University of Technology, 1988.

29. G. D. Seidel, D. H. Allen, K. L. E. Helms, S. E. Groves, *A model for predicting the evolution of damage in viscoelastic particle-reinforced composites*, Mechanics of Materials **37**(1) (2005), 163–178.

30. S. A. Silling, *Reformulation of elasticity theory for discontinuities and long-range forces*, Journal of the Mechanics and Physics of Solids **48**(1) (2000), 175–209.

31. S. A. Silling E. Askari, *A meshfree method based on the peridynamic model of solid mechanics*, Comput. Struct. **83**(17–18) (2005), 1526–1535.

32. S. A. Silling, M. Epton, O. Weckner, J. Xu, E. Askari, *Peridynamic states and constitutive modeling*, J. Elasticity **88**(2) (2007),151–184.

33. J. H. Song, H. Wang, T. Belytschko, *A comparative study on finite element methods for dynamic fracture*, Comput. Mech. **42**(2) (2008), 239–250.

34. N. Sukumar, D. L. Chopp, N. Moës, T. Belytschko, *Modeling holes and inclusions by level sets in the extended finite-element method*, Comput. Methods Appl. Mech. Eng. **190**(46–47) (2001), 6183–6200.

35. Y. Tong, W. Shen, J. Shao, J. Chen, *A new bond model in peridynamics theory for progressive failure in cohesive brittle materials*, Eng. Appl. Fract. Mech. **223** (2020), 106767.

36. P. Underwood, *Dynamic relaxation*, in: T. Belytschko, T. J. R. Hugues (eds.), *Computational Methods for Transient Analysis*, Mechanics and mathematical methods, North-Holland, Amsterdam, 1983, 245–265.

37. V. S. Mutnuri, S. Goapalakrishnan, *A comparative study of wave dispersion between discrete and continuum linear bond-based peridynamics systems: 1D framework*, Mech. Res. Commun. **94** (2018), 40–44.

38. Y. Wang, X. Zhou, M. Kou, *An improved coupled thermo-mechanic bond-based peridynamic model for cracking behaviors in brittle solids subjected to thermal shocks*, Eur. J. Mech., A, Solids **73** (2019), 282–305.

39. T. L. Warren, S. A. Silling, A. Askari, O. Weckner, M. A. Epton, J. Xu, *A non-ordinary state-based peridynamic method to model solid material deformation and fracture*, Int. J. Solids Struct. **46**(5) (2009), 1186–1195.

40. B. Winkler, G. Hofstetter, H. Lehar, *Application of a constitutive model for concrete to the analysis of a precast segmental tunnel lining*, Int. J. Numer. Anal. Methods Geomech. **28**(78) (2004), 797–819.

41. B. Winkler, G. Hofstetter, G. Niederwanger, *Experimental verification of a constitutive model for concrete cracking*, Proceedings of the Institution of Mechanical Engineers, Part L: Journal of Materials: Design and Applications **215**(2) (2001), 75–86.

42. P. Wu, J. Zhao, Z. Chen, F. Bobaru, *Validation of a stochastically homogenized peridynamic model for quasi-static fracture in concrete*, Eng. Appl. Fract. Mech. **237** (2020), 107293.

43. D. Yang, W. Dong, X. Liu, S. Yi, X. He, *Investigation on mode-I crack propagation in concrete using bond-based peridynamics with a new damage model*, Eng. Appl. Fract. Mech. **199** (2018), 567–581.

44. D. Yang, X. He, S. Yi, X. Liu, *An improved ordinary state-based peridynamic model for cohesive crack growth in quasi-brittle materials*, Int. J. Mech. Sci. **153**–**154** (2019), 402–415.

45. H. Yu, X. Chen, *A viscoelastic micropolar peridynamic model for quasi-brittle materials incorporating loading-rate effects*, Comput. Methods Appl. Mech. Eng. **383** (2021), 113897.

46. H. Yu, X. Chen, Y. Sun, *A generalized bond-based peridynamic model for quasi-brittle materials enriched with bond tension–rotation–shear coupling effects*, Comput. Methods Appl. Mech. Eng. **372** (2020), 113405.

47. M. Zaccariotto, F. Luongo, G. Sarego, U. Galvanetto, *Examples of applications of the peridynamic theory to the solution of static equilibrium problems*, The Aeronautical Journal **119**(1216) (2015), 677–700.

48. X. Zhang, H. Wang, *A fast collocation method for a static bond-based linear peridynamic model*, Comput. Methods Appl. Mech. Eng. **311** (2016), 280–303.

49. I. Zreid, M. Kaliske, *Regularization of microplane damage models using an implicit gradient enhancement*, Int. J. Solids Struct. **51**(19-20) (2014), 3480–3489.

НОВИ МОДЕЛ КВАЗИ КРТОГ ОШТЕЋЕЊА ПРИМЕЊЕН У КВАЗИСТАТИЧКИМ УСЛОВИМА КОРИШЋЕЊЕМ ПЕРИДИНАМИЧКЕ ТЕОРИЈЕ ЗА ПРОГРЕСИВНИ ЛОМ

РЕЗИМЕ. Предложен је нови модел квази кртог оштећења примењен у условима квазистатичког оптерећења користећи перидинамичку теорију за прогресивни лом да би се боље предвидео почетак и ширење оштећења у чврстим материјалима. Пошто је перидинамичка једначина кретања изведена у динамичкој конфигурацији, у овом раду се примењује прилагођена једначина динамичке релаксације да би се постигло стационарно стање у перидинамичкој формулацији. Да бисмо прецизно окарактерисали процес прогресивног лома у кохезивним материјалима, примењујемо динамичку једначину са новим моделом оштећења за квази крте материјале. Приказани су рачунарски примери 2Д компресивних и затезних проблема применом предложеног модела. Овај рад представља напредак уградњом приступа прилагођене динамичке једначине у нови модел оштећења квази кртих материјала. Ово спајање омогућава прецизније представљање понашања оштећених материјала, посебно при статичким или квазистатичким оптерећењима, приближавајући модел реалном проблему. Ово истраживање отвара пут да се перидинамичка формулација користи за далеко ширу класу услова оптерећења него што је то сада у могућности.

Faculty of Mechanical and Automotive Engineering Technology   (Received 04.04.2023)
University Malaysia Pahang   (Revised 22.05.2023)
Pekan   (Available online 16.06.2023)
Pahang
Malaysia
pmv20001@student.ump.edu.my

Faculty of Mechanical and Automotive Engineering Technology
University Malaysia Pahang
Pekan
Pahang
Malaysia
nikabdullah@ump.edu.my

Faculty of Mechanical and Automotive Engineering Technology
University Malaysia Pahang
Pekan
Pahang
Malaysia
ruzaimi@ump.edu.my

Faculty of Civil Engineering Technology
University Malaysia Perlis
Arau
Perlis
Malaysia
aniraasyikin@unimap.edu.my